Combustion Science and Technology

A NUMERICAL INVESTIGATION OF METHANE AIR PARTIALLY PREMIXED FLAMES AT ELEVATED PRESSURES

PLEASE SCROLL DOWN FOR ARTICLE

Taylor & Francis
Taylor & Francis Group

A Numerical Investigation of Methane Air Partially Premixed Flames at Elevated Pressures

Sibendu Som and Suresh K. Aggarwal[*]

Department of Mechanical and Industrial Engineering, University of Illinois at Chicago, Chicago, IL, USA

Abstract: A numerical investigation of high pressure, counterflow methane-air partially premixed flames (PPFs) is presented to characterize the effect of pressure on flame structure. Four different mechanisms, namely GRI-2.11, GRI-3.0, the San Diego, and the C_2 mechanisms have been examined. The mechanisms have been validated by comparing the predicted laminar flame speeds with experimental data. While there is excellent agreement between the measured and predicted laminar flame speeds based on these mechanisms, there are noticeable discrepancies amongst the mechanisms for the prediction of high-pressure PPFs. The GRI 3.0 mechanism is used to examine the detailed PPF structure at elevated pressures. At low pressures, the PPF exhibits a typical double flame structure that consists of rich premixed and nonpremixed reaction zones, and the separation distance between the reaction zones decreases with increasing pressure. However, for pressure above 10 atm, the separation distance becomes nearly independent of pressure. In addition, a critical pressure is observed, above which the PPF structure exhibits anomalous behavior, characterized by the presence of endothermic reactions and the production of CO in the region between the two reaction zones. A rate of production analysis revealed that the anomalous behavior is attributable to the following reactions: $H + H_2O \rightarrow OH + H_2$, $CH_2CO + M \rightarrow CH_2 + CO + M$, and $HCO + M \rightarrow H + CO + M$. The critical pressure at which this behavior is first observed increases with the increase in equivalence ratio and/or

strain rate. Thermal radiation is found to have a negligible effect on the flame structure for the range of conditions investigated.

INTRODUCTION

In recent years, there has been significant interest in the study of partially premixed flames (PPFs). Typically, PPFs are established by mixing less than stoichiometric amount of air with a fuel stream, and supplying additional air from another stream. For instance a PPF can be established in a coflowing configuration, with the inner flow containing a fuel-rich mixture and the outer flow containing air (Gore et al., 1996; Azzoni et al., 1999; Shu et al., 1999; Bennett et al., 2000; Shu et al., 2000; Choi et al., 2001). Similarly, one can establish a PPF in a counterflow configuration using two opposing jets, one containing fuel-rich mixture and other containing air (Tanoff et al., 1996; Blevins et al., 1999; Lockett et al., 1999; Barlow et al., 2001; Xue et al., 2001; Xue and Aggarwal, 2002; Xue et al., 2002; Zhu et al., 2002). Partially premixed flames occur in many practical systems, including gas turbine combustors, spark ignition (Flynn et al., 1999) and diesel engines (Lee et al., 1997). Partial premixing is an important process in lifted nonpremixed laminar and turbulent flames (Rogg et al., 1986; Smooke et al., 1988). Irrespective of the configuration or system, a PPF contains two or more reaction zones that are synergistically coupled. For example, in a methane-air PPF containing two reaction zones, the fuel is consumed in the rich premixed zone producing the "intermediate fuels," such as CO and H_2, which are then transported to and consumed in the nonpremixed zone. The latter zone in turn provides heat and radical species to the rich premixed zone. As a result of these interactions, PPFs flames can exploit the advantages of both nonpremixed and premixed flames with regards to safety and flame stability, and also provide higher energy output with lower emissions (Xue et al., 2001).

Combustion in many important applications, such as diesel engines and gas turbine combustors, occurs at high pressures and involve PPFs. However, most previous high-pressure studies have considered premixed or non-premixed flames. Hassan et al., (1998) investigated the effect of positive flame stretch on the burning velocities of methane-air spherical laminar premixed flames for a pressure range of 0.5–4.0 atm. Gu et al. (2000) determined the unstretched laminar burning velocity and Markstein lengths for spherically expanding flames up to 10 atm. They observed that as the pressure increases, the Markstein length for lean

and stoichiometric methane/air flames changes its sign from positive to negative. Kwon and Faeth (2001) showed that at fuel-lean conditions increasing flame temperatures tend to reduce the flame sensitivity to stretch, whereas increasing pressures tend to increase preferential-diffusion instabilities.

Kwon et al. (2002) demonstrated that hydrodynamic instability is greatly enhanced with increasing pressure; although the influence can be moderated by the progressively important three-body termination reactions as the pressure increases. Rozenchan et al. (2002) measured the unstretched laminar burning velocity for methane/air-premixed flames up to 20 atm, and for methane/oxygen/helium flames up to 60 atm. Jomaas et al. (2004) determined the counterflow ignition temperatures and laminar flame speeds of C_2-C_3 hydrocarbons up to 7 atm. Thomsen et al. (1999) modeled the NO formation in premixed, high-pressure methane flames and demonstrated that the GRI 2.11 mechanism is not suitable for quantitative predictions of NO concentrations. Sohn et al. (2002) reported a numerical investigation for NO formation for counterflow methane/diluted air flame at high pressure. Previous investigations on high-pressure nonpremixed flames have focused on the effect of pressure on their topology, structure (Park et al., 2001), ignition (Papas et al., 1994), and emission characteristics (Takagi et al., 1995).

Our literature review of previous investigations on high-pressure flames is summarized in Table 1. As indicated in this table, most previous studies have considered premixed flames, while some have considered non-premixed flames. However, high-pressure PPFs have not been investigated, except for one recent study dealing with H_2-air PPF at high pressure (Briones et al., 2004). Consequently, there are important gaps in our basic understanding of this important class of flames.

OBJECTIVES

The major objective of the present study is to investigate the structure of methane-air PPFs at high pressure. A PPF containing two reaction zones in a counteflow configuration is considered so that the effect of pressure on the flame topology, detailed chemical structure, and interactions between the reaction zones can be examined in a comprehensive manner. Another objective is to evaluate the existing detailed methane-air chemistry models using high pressures PPFs. Methane-air chemistry has been extensively investigated in recent years, and several detailed reaction mechanisms have been developed. These include GRI-3.0 mechanism (Smith et al., 1999), which is the updated version of GRI-2.11 mechanism (Bowman et al., 1995), the San Diego mechanism (2003), the Konnov

Table 1. Available literature on high-pressure flames

Configuration	Pressure range (atm)	Experimental/ Numerical	Fuel type	Reference
Counterflow nonpremixed flames	1–20	Numerical	Methane and diluted Air	Sohn et al. (2002)
Freely propagating premixed flames	1–14.6	Both	Lean premixed methane-air flames	Thomsen et al. (1999)
Counterflow nonpremixed flames	1–100	Numerical	Undiluted Hydrogen Oxygen	Sohn et al. (1998)
Outwardly propagating spherical flames	0.35–4.0	Both	$H_2/O_2/N_2$ ($\phi = 0.45$–4.0)	Aung et al. (1998)
Counterflow PPFs	1–13	Numerical	Undiluted Hydrogen Oxygen	Briones et al. (2004)
Outwardly propagating spherical flames	0.3–3.0	Both	$H_2/O_2/$(air, He or Ar) ($\phi = 0.6$–4.5)	Kwon and Faeth (2001)
Outwardly propagating spherical flames	1, 3, 5, 10, 15, 20	Both	$H_2/O_2/He$ ($\phi = 0.5$–3.5)	Tse et al. (2000)
Outwardly propagating spherical flames	1–20 20–60	Both	CH_4-Air $CH_4/O_2/He$	Rozenchan et al. (2002)
Counterflow nonpremixed ignition	4	Both	9% H_2–91%N_2	Fotache et al. (1998)
Freely propagating spherical premixed flames	0.5–4	Both	CH_4-Air	Hassan et al. (1998)

mechanism (Konnov, 2000), the Leeds mechanism (2001) and the C_2 mechanism (Peters et al., 1993).

In previous studies, various mechanisms have been evaluated using a variety of systems, such as flow reactor, shock tube, stirred reactor, freely propagating flames, and nonpremixed flames. However, the PPFs have generally not been employed. Since a PPF possesses the characteristics of both premixed and nonpremixed flames, and its structure depends strongly on the transport of radical and intermediate species between the various reaction zones (Azzoni et al., 1999), it is ideally suited for validating a given reaction mechanism, as well as for identifying the dominant reaction pathways in the mechanism. Moreover, since the flame structure and interactions between the reaction zones can be modified by changing the equivalence ratio, flow velocity, and pressure, a reaction mechanism can be validated for a wide range of conditions, including limiting conditions, using high-pressure PPFs.

In the present study, we have examined the GRI 2.11, GRI 3.0, San Diego and C_2 mechanisms for predicting the structure of methane-air PPFs at elevated pressures. Since there have not been any experimental studies concerning high-pressure methane-air PPFs, these mechanisms are first examined for predicting the laminar flame speeds for methane-air mixtures at different pressures. The GRI-2.11 mechanism (Bowman et al., 1995) involves 277 elementary reactions and 49 species, while the GRI-3.0 mechanism (Smith et al., 1999), involves 325 elementary reactions and 53 species. Rozenchan et al. (2002) have observed good agreement with the measured laminar burning velocities of methane air mixtures at elevated pressures using the GRI 3.0 mechanism. The GRI 3.0 mechanism without the NO_x chemistry has 216 elementary reactions with 37 species. The San Diego mechanism (2003) contains 173 reactions and 39 species, while the C_2 mechanism (Peter et al., 1993) contains 81 elementary reactions and 24 species. The San Diego mechanism has previously been validated by Li et al. (1999) for counterflow methane-air PPFs at atmospheric pressure. The C_2 mechanism has been validated for both counterflow (Xue et al., 2002) and coflow (Shu et al., 1998; Azzoni et al., 1999) methane-air PPFs at atmospheric pressure.

The paper is organized as follow. First the numerical model is described. The four mechanisms are then validated using measurements for freely propagating laminar premixed flames at different pressures. This is followed by the comparison of these mechanisms in predicting the structures of PPFs at different pressures. The GRI 3.0 mechanism is then used to characterize the effect of pressure on the detailed structure of methane-air PPFs. The effect of pressure on the dominant reaction pathways is also characterized. Finally the conclusions are presented.

NUMERICAL MODEL

The counterflow flame configuration employed in the present investigation is shown schematically in Figure 1. It consists of two opposing jets issuing from two coaxial nozzles that are placed one above the other. A rich methane-air mixture flows from the lower nozzle and air from the upper nozzle. The separation distance between the nozzles is 1.27 cm. PPFs are established at different pressures by independently varying the fuel stream equivalence ratio (ϕ) and the global strain rate. The global strain rate (Vagelopoulos et al., 1994) is expressed as $a_s = (2|v_o|/L) \cdot \{1 + |v_f|\sqrt{\rho_f}/|v_o|\sqrt{\rho_o}\}$ where, L denotes the separation distance between the two jets, v_o the oxidizer jet inlet velocity, v_f the fuel jet inlet velocity, and ρ_f and ρ_o are the mixture densities in the fuel and oxidizer streams, respectively. The inlet velocities of the fuel and oxidizer streams are obtained by matching the momenta of the two streams for given ϕ and a_s. The effect of radiation is included by using an optically thin radiation model. The Soret and Dufour effects are neglected.

Simulations of methane-air PPFs at a given ϕ, a_s and pressure (p) are performed using the OPPDIF (Lutz et al., 1996) code in the CHEMKIN package (Kee et al., 1996). The temperatures of the fuel and oxidizer nozzles are set at 300 K. The grid independence of the results was achieved by controlling the values of the GRAD and CURV parameters, using adaptive re-gridding in order to resolve the structures of both the
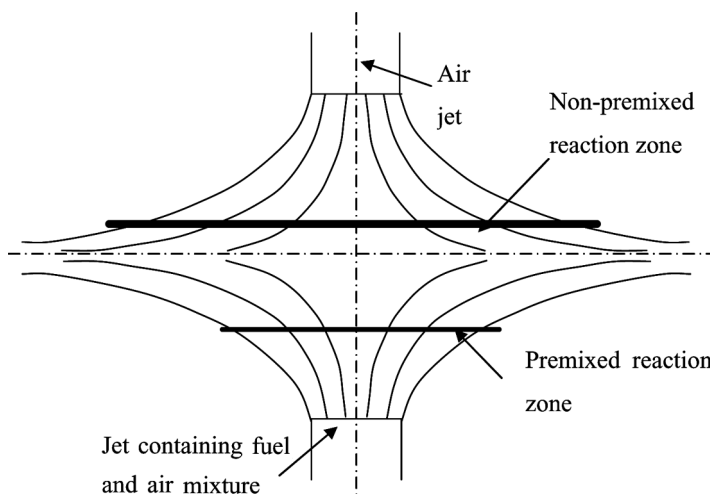

Figure 1. A schematic of the counterflow flame configuration used in the present study.

premixed and nonpremixed reaction zones. This required the number of grid points to be 250 for the base case at 1 atm. At high pressures the thickness of both the rich premixed and nonpremixed zones decreases, and thus the number of grid points required to obtain a grid independent solution also increases. A satisfactory resolution at the highest pressure investigated required 550 grid points.

RESULTS AND DISCUSSION

Validation

Since measurements of high-pressure methane-air PPFs are yet to be reported, it is difficult to select a reliable mechanism for the present investigation. However, laminar burning velocity data for premixed methane-air mixtures at pressures up to 20 atm has been reported by Rozenchan et al. (2002). These data are used to validate the four reaction mechanisms mentioned earlier. In Figure 2a we plot the measured and predicted laminar burning velocities as function of pressure. The mixture temperature and equivalence ratio are 300 K and 1.0, respectively. The numerical results obtained using these four mechanisms show excellent agreement with measurements. For pressure up to 10 atm, the unstretched laminar flame speed (S_u^0) decreases rapidly with increasing pressure, and thereafter exhibits a weak dependence on p. S_u^0 as a function of p can be expressed as $S_u^0 = p^{(n/2)-1}$ (Egolfopoulos et al., 1990), where (n) is the overall reaction order and computed from:

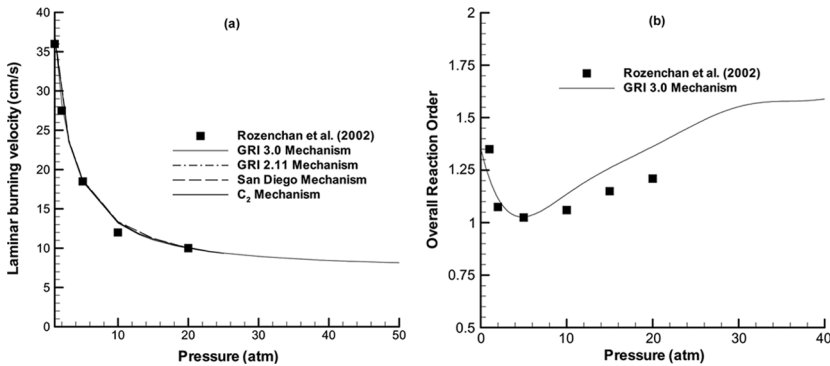$$n = 2 + 2\left(\frac{\partial \ln(S_u^0)}{\partial \ln(p)}\right)$$

Figure 2. Variation of measured and predicted laminar burning velocity (a) and overall reaction order (b) with pressure for various mechanisms for a methane air premixed mixture at $\phi = 1.0$.

Figure 2b presents n as a function of pressure. Since the values of n predicted by the four mechanisms were essentially the same for pressure range of 1–40 atm, results are only shown for GRI 3.0 mechanism. For these results, $n < 2$, and consequently, the unstretched laminar burning velocity decreases with pressure (cf. Figure 2a). At higher pressures, however, the laminar burning velocity becomes nearly independent of pressure, and n asymptotically approaches a value of 2, as indicated in Figure 2b. These results agree well with the measurements reported by Rozenchan et al. (2002). An important observation from Figures 2a and 2b is that all four mechanisms are able to reproduce the measured laminar burning velocities as a function of pressure. Since, the C_2 mechanism is computationally more efficient, it may be used to predict the laminar burning velocities at high pressure.

Effect of Radiation on the Structure of PPF

Barlow et al. (2001) observed that radiation plays an important role on NO formation at low strain rates. Pogliani et al. (2001) reported a numerical investigation of atmospheric methane-air nonpremixed flames to examine the effects of radiation and dilution on flame extinction. The extinction characteristics of weakly strained flames were found to be significantly influenced by radiation. However, the effect of radiation was found to be negligible at high strain rates due to small residence time. In the present study, an optically thin radiation model is employed to characterize the effect of thermal radiation on the PPF structure at different pressures. Figure 3 presents temperature profiles for methane-air PPFs computed with and without radiation at different pressures. The GRI-3.0 mechanism is used for these simulations. Results indicate that the effect of radiation on the computed flame structure is negligible.

Effect of Pressure on PPF Structure: Comparison of Reaction Mechanisms

The grid independence was achieved by controlling the values of the GRAD and CURV parameters and using adaptive re-gridding in order to resolve the structures of both the premixed and nonpremixed reaction zones. The grid independence was ensured by increasing the number of grid points to 1.5 times the original value, and comparing predictions for the two grids. The results presented in this paper employed 250 grid points at 1 atm, and 550 grid points at 20 atm.

In order to compare the four reaction mechanisms, we computed the methane-air PPF for the base case, i.e., $a_s = 100 \, s^{-1}$ and $\phi = 1.4$, at
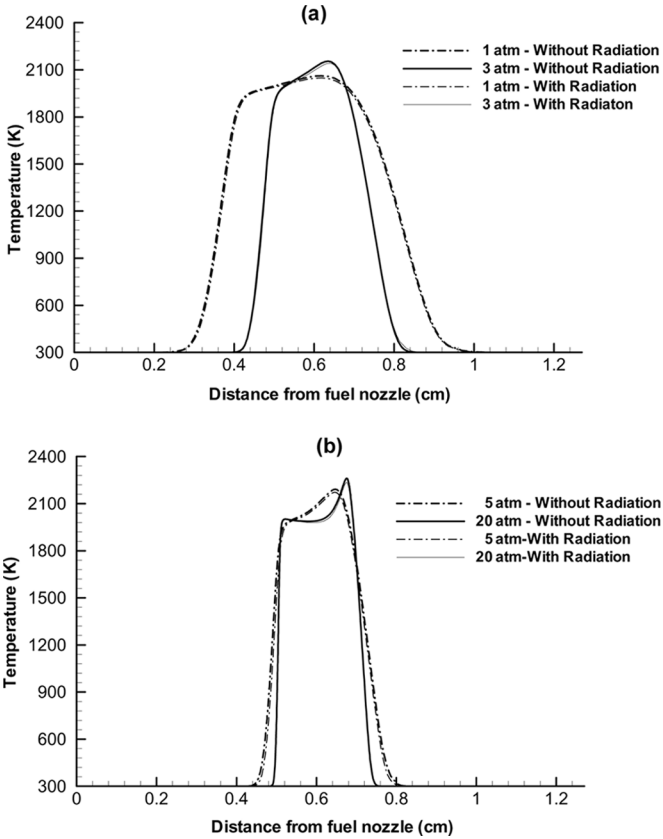
Figure 3. Temperature profiles for methane air PPFs established at $\phi = 1.4$, $a_s = 100\,s^{-1}$, and different pressures, and computed with and without the radiation model.

different pressures. Figure 4 presents temperature profiles computed using the four mechanisms at different pressures. At p = 1 atm, the temperature profiles exhibit a qualitatively similar flame structure for all four mechanisms, except that the C_2 mechanism predicts a narrower flame compared to the other three mechanisms. The flame structure is characterized by the presence of two reaction zones, namely a rich premixed zone on the fuel side and a nonpremixed zone on the air side. As expected, the thickness of both reaction zones decreases with increasing p (Halter et al., 2004). In addition, as p increases, the separation distance between the two reaction zones decreases, which can be attributed to the effect of p on laminar flame speed. The flame speed associated with the rich premixed zone decreases with increasing p, and, consequently,
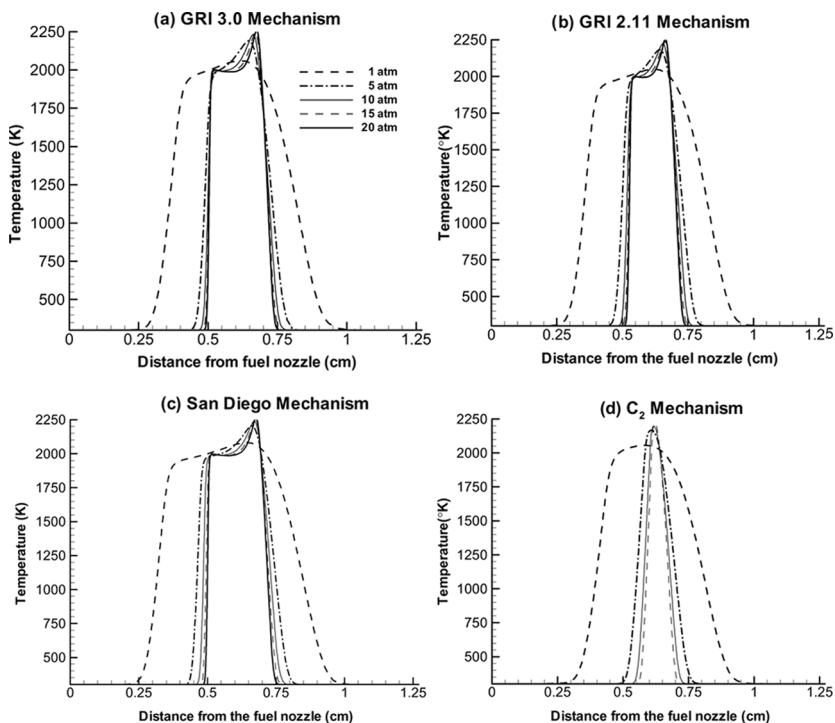
Figure 4. Temperature profiles at different pressures for methane-air PPFs established at $\phi = 1.4$, $a_s = 100\,s^{-1}$ and computed using GRI 3.0 mechanism (a), GRI 2.11 mechanism (b), San Diego mechanism (c) and C_2 mechanism (d).

this zone moves downstream to a location where the axial flow velocity matches the stretched laminar flame speed. However, as discussed later, this trend continues only for pressures upto 10 atm.

Another important observation from Figure 4 is that the temperature profiles for C_2 mechanism exhibit significant differences with those for the other three mechanisms, and these differences become more pronounced at higher pressures. For example, even at 1 atm, the temperature profile for C_2 mechanism indicates a relatively narrower PPF compared to those for other mechanisms. In addition, the C_2 mechanism yields a nearly merged flame structure at 5 atm whereas the other mechanisms predict flames with two distinct reaction zones even at higher pressures.

The effect of pressure on the stretched flame speed and the location of the rich premixed zone is shown more clearly in Figure 5, which presents the axial velocity profiles computed using the GRI-3.0 mechanism at different pressures. It is seen that the stretched laminar flame speed, which is defined by the minimum value of the flow velocity upstream
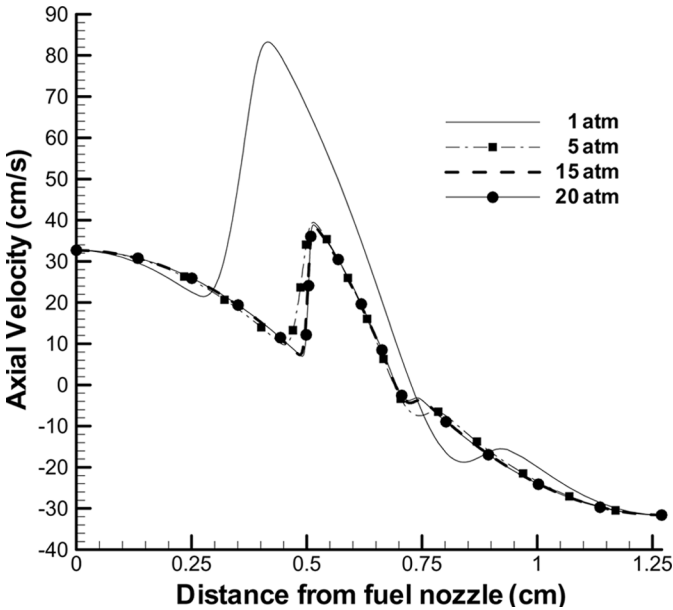
Figure 5. Axial velocity profiles for methane-air PPFs discussed in the context of Figure 4.

of the rich premixed zone, decreases rapidly (from 22 cm/s to 10 cm/s) as pressure is increased from 1 to 10 atm, and thereafter becomes nearly independent of pressure. The stretched and unstretched laminar burning velocities are related as (Markstein, 1964): $S_u = S_u^0 - LK$, where S_u denotes the stretched laminar burning velocity, L the Markstein length, and K the flame stretch. In the limit of small stretch (Leis et al., 1969), this equation is simplified to $S_u = S_u^0(1 - Ma_\infty Ka_\infty)$, where Ka_∞ denoted the Karlovitz number representing the flame stretch and Ma_∞ the Markstein number representing the sensitivity of laminar flame speed to stretch. Thus, as the unstretched flame speed decreases with pressure, the stretched flame speed would also decrease causing the premixed reaction zone to move away from the fuel nozzle so as to balance the local flow velocity. As indicated in Figure 5, the stretched laminar flame speed decreases rapidly as p is increased from 1 to 10 atm, but then becomes nearly independent of pressure, which is consistent with the variation of unstretched flame speed with p shown in Figure 2a. As a consequence, the separation distance between the two reaction zones decreases rapidly as p increases from 1 to 10 atm, but then becomes nearly independent of pressure for p>10 atm.

Figure 6 presents the heat release rate profiles predicted by the four mechanisms at different pressures. The two peaks in the heat release rate
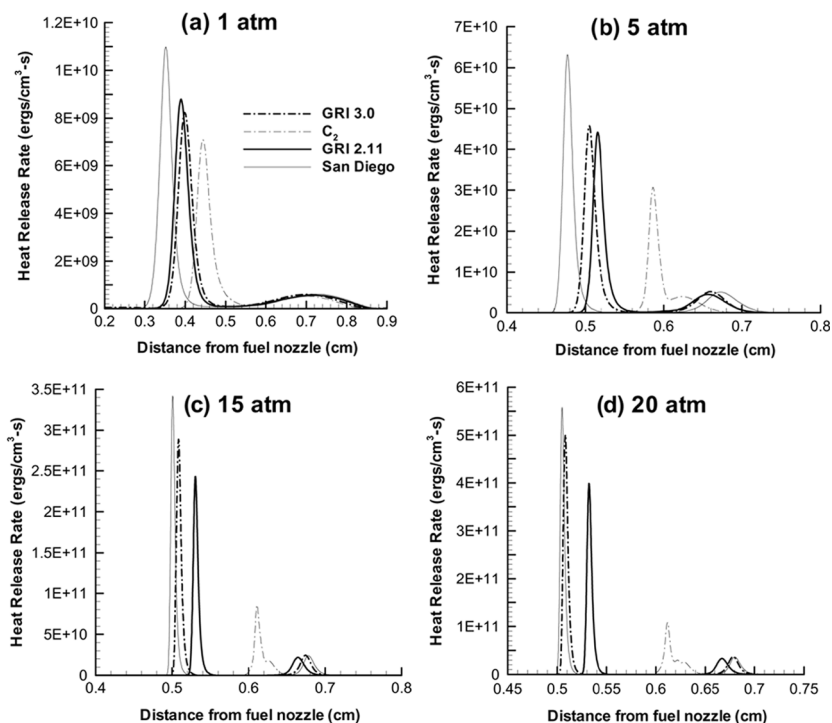
Figure 6. Heat release rate profiles for methane-air PPFs established at $\phi = 1.4$, $a_s = 100\,s^{-1}$, and computed using GRI 3.0, GRI 2.11, San Diego and C_2 mechanisms at 1 atm (a), 5 atm (b), 15 atm (c) and 20 atm.

profile locate the premixed and nonpremixed reaction zones. The values of these peaks increase as p is increased. This is expected since the thickness of both the reaction zones decreases, and the fuel and oxidizer flow rates increase as p is increased. A more important observation from Figure 6 pertains to the marked differences in the heat release rate profiles predicted by the GRI 3.0, GRI 2.11 and San Diego mechanisms, although the corresponding temperature profiles appear to be similar. The differences in the heat release rates are more significant in the rich premixed zone compared to those in the nonpremixed zone, underlining differences in the chemistry models for rich methane-air mixtures. The San Diego mechanism predicts consistently higher heat release rate compared to the other mechanisms. In addition at lower pressures (p = 1 and 5 atm), the heat release rate profiles predicted by the GRI 2.11 and GRI 3.0 mechanisms are similar, while at higher pressures (p = 15 and 20 atm), those predicted by the GRI 3.0 and San Diego mechanisms become similar. These differences clearly highlight the need for further

work on developing high-pressure methane-air chemistry models and validating these models using PPFs.

PPF Structure at Elevated Pressures

Previous numerical and experimental investigations of PPFs at one atmosphere have shown that in the region between the two reaction zones, the temperature increases monotonically from the rich premixed to the nonpremixed reaction zone. However, our results indicate that the temperature variation in this region is monotonic at low pressure, but becomes non-monotonic at high pressure. This is shown more clearly in Figure 7, which presents a zoomed view of the region between the two reaction zones at various pressures. As expected, the thickness of the rich premixed zone decreases and its peak temperature increases with increasing pressure. This is consistent with the results for the corresponding premixed flame, shown in terms of the variation of the maximum
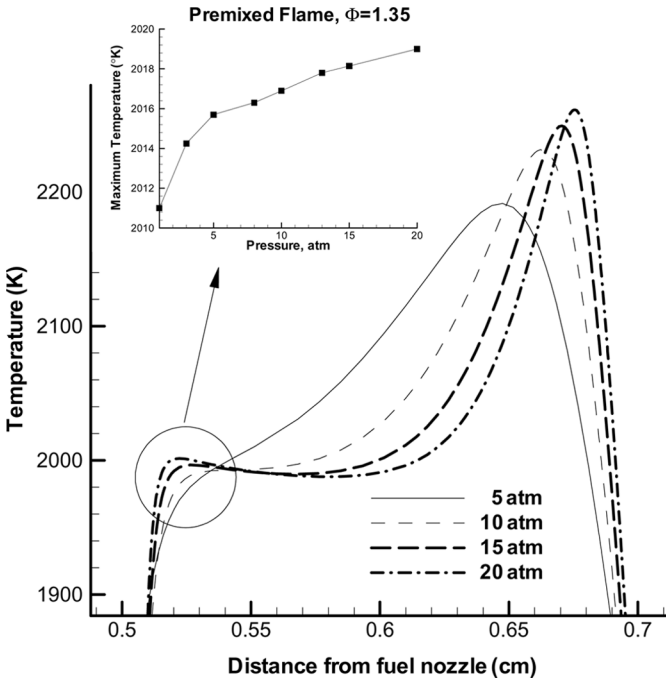

Figure 7. Zoomed view of the region between the two reaction zones for methane-air PPFs discussed in the context of Fig. 4. The maximum temperature for the corresponding premixed methane-air flames at $\phi = 1.35$ as a function of pressure is shown in the inset.

temperature with pressure in the inset of Figure 7. A more important observation from Figure 7 is that the temperature profiles between the two reaction zones exhibit a monotonic variation at low pressure ($p \leq 10$ atm), but a non-monotonic variation at high pressure ($p > 10$ atm). A detailed analysis indicated that this anomalous behavior occurs at $p \geq 11$ atm, and involves the presence of endothermic reactions that become important above this pressure.

In order to gain further insight into this anomalous behavior, we present in Figures 8 and 9 the mole fraction profiles of several species for PPFs discussed in the context of Fig. 4 and 7. For all the cases depicted in Figure 8, methane is almost completely consumed in the rich premixed zone, in accordance with previously published results for PPFs at one atmosphere (Blevins et al., 1999; Xue et al., 2002). These profiles also indicate that as the pressure increases, the rich premixed zone moves downstream and its thickness decreases. A similar behavior is exhibited by O_2 profiles in both the rich premixed and nonpremixed zones. About 80% of oxygen is consumed by the reaction (R38), $H + O_2 \rightarrow OH + O$ in the rich premixed zone, while 100% of oxygen is consumed by this reaction in the nonpremixed zone. This is in accordance with the results
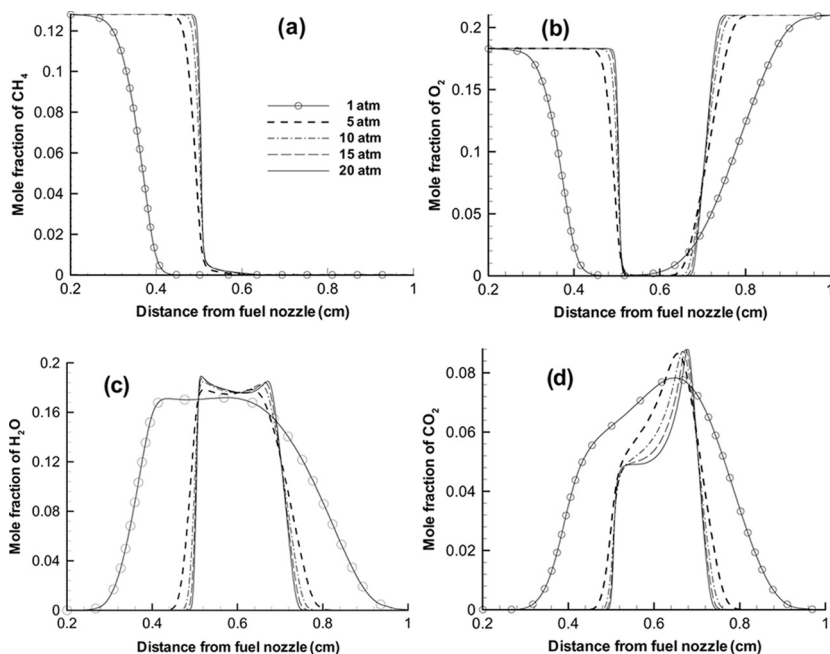

Figure 8. Mole fraction profiles of CH_4 (a), O_2 (b), CO_2 (c) and H_2O (d) at different pressures for flames discussed in the context of Figure 4.
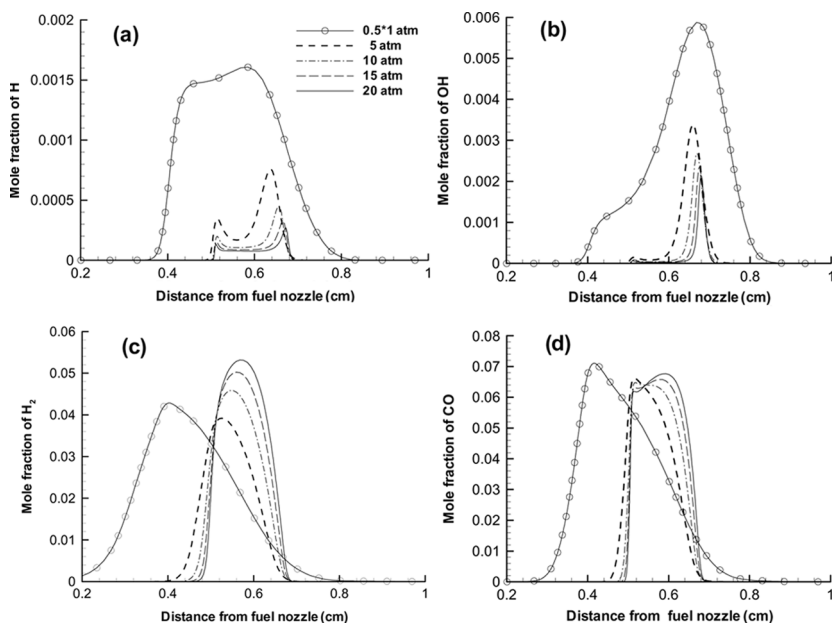
Figure 9. Mole fraction profiles of H (a), H_2 (b), CO (c) and OH (d) at different pressures for flames discussed in the context of Figures 4 and 6.

reported by Gardiner (1984). The H_2O profiles exhibit two distinct peaks, corresponding to the two reaction zones. The H_2O mole fraction increases with increasing pressure, which is mainly due to reaction R84: $OH + H_2 \rightarrow H + H_2O$, whose rate increases with pressure. However, in the region between the two reaction zones, as the pressure is increased, the direction of this reaction is reversed due to the low concentration of OH radical in this region. Consequently, the H_2O mole fraction decreases in this region, and the effect becomes more pronounced at higher pressures, as indicated in Figure 8c.

The CO_2 profiles are qualitatively similar to the temperature profiles in that they exhibit two peaks corresponding to the two reaction zones, and that there is consumption of CO_2 in the region between the two reaction zones. Reactions involving CO and CO_2 are key reactions in hydrocarbon combustion, since CO appears as the intermediate product of hydrocarbon oxidation and is subsequently converted to CO_2. There are two reactions that cause CO oxidation, namely $CO + O + M \rightarrow CO_2 + M$ and $CO + OH \rightarrow CO_2 + H$. The first reaction is not important as long as even small quantities of hydrogen-containing radicals are available. In hydrocarbon flames, typically 99.9% of CO oxidation occurs due to the second reaction (Gardiner, 1984). The local CO_2 peak in the rich

premixed zone decreases slightly with increasing pressure while it increases with pressure in the nonpremixed zone. This is due to the decrease in OH concentration in the premixed reaction zone at high pressure. There is also a decrease in CO_2 mole fraction between the two reactions zones, which provides another evidence of endothermicity in this region. This also implies an increase in CO mole fraction in this region, as discussed later.

Figure 9 presents mole fraction profiles of H, OH, H_2, and CO at different pressures. Both H and OH profiles exhibit two peaks corresponding to the two reaction zones. In addition, the peak mole fractions of both radicals are higher in the nonpremixed zone compared to those in the rich premixed zone. This is due to the domination of H_2/O_2 chemistry in the former zone. As the pressure is increased, the mole fractions of these radical species decrease, which is in accordance with previously published results (Sohn et al., 2000). In addition, the H radical profiles indicate that as the pressure is increased, the nonpremixed zone first moves toward the rich premixed zone, and then moves away from it. The H_2 mole fraction profiles indicate that H_2 is produced in the rich premixed zone, and then transported to and consumed in the nonpremixed zone. As the pressure increases, the peak H_2 mole fraction first decreases and then increases. At low pressures, the dominant H_2 production reaction is $H + CH_4 \rightarrow CH_3 + H_2$ (R53), while the dominant consumption reactions are $O + H_2 \rightarrow H + OH$ (R3) and $OH + H_2 \rightarrow H + H_2O$ (R84). As the pressure increases, the rates of reactions R3 and R84 increase at a faster rate than that of R53, and, consequently, the H_2 peak initially decreases with pressure. However, at high pressures, other H abstraction reactions, namely $H + CH_2O \rightarrow HCO + H_2$ (R58), $H + C_2H_4 \rightarrow C_2H_3 + H_2$ (R75) and $H + C_2H_6 \rightarrow C_2H_5 + H_2$ (R78) become important, and the H_2 peak then increases with pressure.

The CO profiles exhibit a typical PPF structure at low pressures, i.e., CO is produced in the rich premixed zone, and then transported to and consumed in the nonpremixed zone. However, at high pressures ($p > 10$ atm), the CO profiles exhibit an anomalous behavior, characterized by the production of CO, in the region between the two reaction zones. As a consequence, the CO profiles have two peaks at high pressures, with the first peak occurring in the rich premixed zone and the second peak between the two reaction zones. Since, for $p > 10$ atm, the temperature profiles also indicate an anomalous behavior, characterized by a decrease in temperature, in the same region (cf. Figure 7), the implication is that the anomalous behavior is associated with some endothermic reactions that become important at high pressures, and produce CO in this region. This is clearly illustrated in Figure 10, which presents the temperature and CO mole fraction profiles for PPFs established at 15 and 20 atm. These profiles indicate a direct correlation
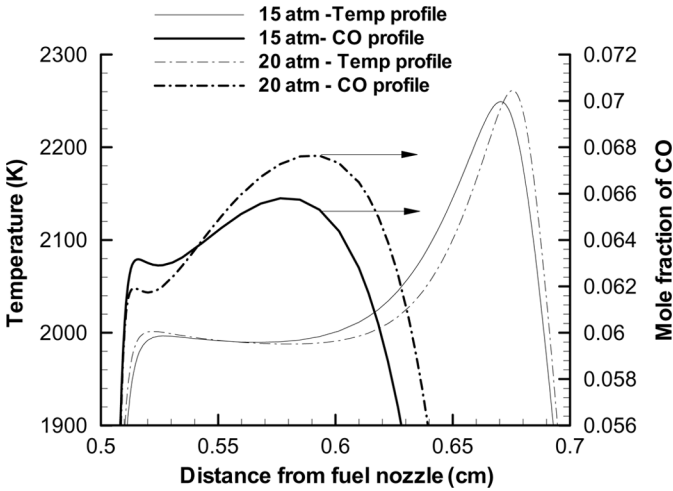
Figure 10. Zoomed view of the flame structure between the reaction zones, shown in terms of the temperature and CO mole fraction profiles, for PPFs discussed in the context of Figure 4.

between the decrease in temperature and the increase in CO mole fraction in the endothermic region downstream of the rich premixed zone. Moreover, as the pressure is increased, both the extent of endothermic region and the degree of endothermicity increase.

A rate of production analysis (ROPA) (Turanyi, 2003) was performed to identify reactions responsible for this anomalous behavior. The analysis yielded the following two reactions responsible for the observed endothermicity; R84: $OH + H_2 \Leftrightarrow H + H_2O$, and R140: $CH_2CO(+M) \Leftrightarrow CH_2 + CO(+M)$. Figure 11 presents heat release rate profiles associated with these two reactions as well as the net heat release rate profile for PPFs established at 5 and 20 atm. At $p = 5$ atm, the net heat release rate profile exhibits two peaks corresponding to the two reaction zones. The heat release rate profiles for reactions R84 and R140 also exhibit two peaks in the two reaction zones, except that R84 reaction is exothermic while R140 is endothermic. These profiles also indicate that in the region between the two reaction zones, the heat release rates are nearly zero, implying insignificant chemical activity in this region; a zoomed view of this region is presented in Figure 11c. However, at $p = 20$ atm, the heat release rates have non-negligible negative values in the region downstream of the premixed zone, indicating endothermicity in this region; a zoomed view of this region is shown in Figure 11d. This endothermicity is consistent with the decrease in temperature and increase in CO mole fraction discussed in the context of Figure 10.
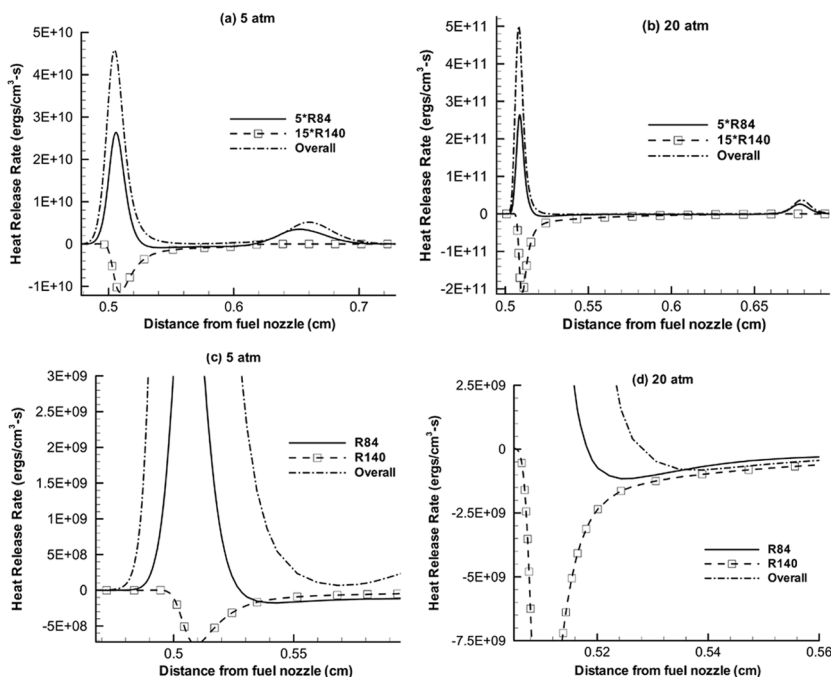
Figure 11. Profiles of net heat release rate and heat release rates by reactions R84 and R140 at 5 atm (a) and 20 atm (b) for flames discussed in the context of Figure 4. Zoomed views of the region between the two reaction zones at 5 atm and 20 atm are shown in Figures 11(c) and 11(d), respectively.

It is also important to note that for reaction R140, the forward reaction dominates and is endothermic at all pressures. However, for reaction R84, the forward reaction is exothermic and dominates at low pressures (p = 5 atm), while at high pressures (p > 10 atm), the endothermic backward reaction dominates between the reaction zones. Another evidence for the reversal of this reaction at high pressures is provided by the fact that at high pressures (p > 10 atm), the mole fraction of H_2 increases (cf. Figure 9), while that of H_2O decreases in region between the reaction zones (cf. Figure 8). Thus, the observed endothermicity at high pressures is caused by reactions R84 and R140, and the magnitude of endothermicity increases with increasing pressure. Moreover, since reaction R140 produces CO, it also contributes to the observed increase in CO mole fraction downstream of the rich premixed zone.

ROPA (Turanyi, 2003) was also used to identify reactions responsible for the observed increase in CO concentration between the two reaction zones. It yielded the following dominant reactions associated

with the production and consumption of CO:

$$OH + CO \Leftrightarrow H + CO_2 \tag{R99}$$

$$CH_2CO + M \Leftrightarrow CH_2 + CO + M \tag{R140}$$

$$HCO + H_2O \Leftrightarrow H + CO + H_2O \tag{R166}$$

$$HCO + M \Leftrightarrow H + CO + M \tag{R167}$$

$$HCO + O_2 \Leftrightarrow HO_2 + CO \tag{R168}$$

$$HCCO + O_2 \Leftrightarrow OH + 2CO \tag{R176}$$
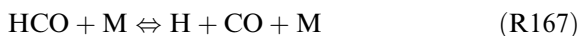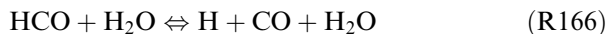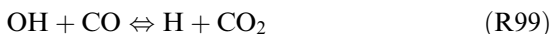
Figure 12 presents the reaction rate profiles of these reactions and the net CO production/consumption for PPFs established at 5 and 20 atm. For both p = 5 and 20 atm, CO is mainly produced in the rich premixed zone
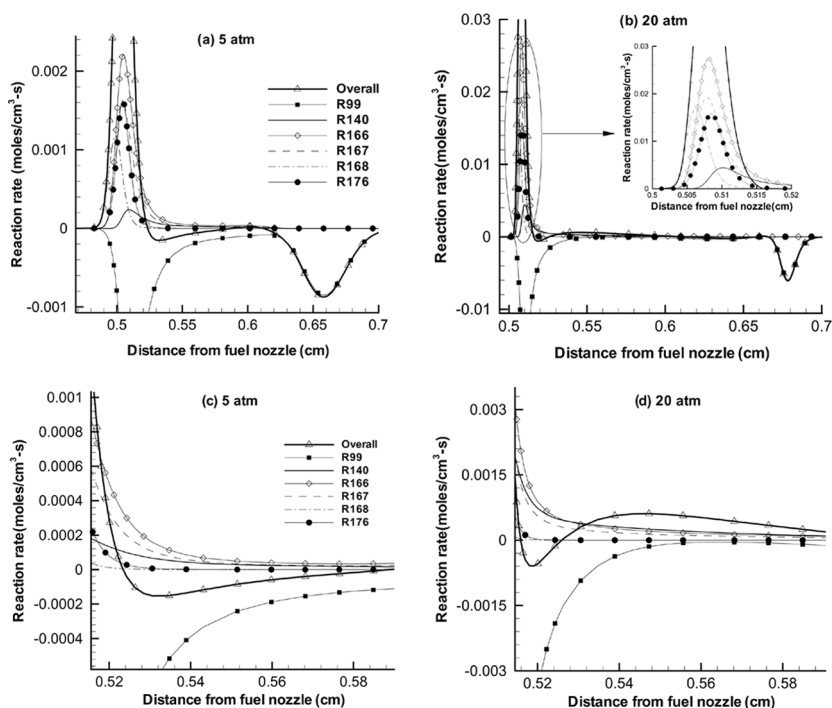
Figure 12. Net CO production/consumption rate and CO production/ consumption rates by reactions R99, R140, R166, R167, R168 and R176 at 5 atm (a) and 20 atm (b) for flames discussed in the context of Figures 4 and 11. Zoomed views of the region between the two reaction zones at 5 atm and 20 atm are shown in Figures 12(c) and 12(d), respectively.

and consumed in the nonpremixed zone. The dominant CO production reactions are R166, R167, R168, and R176, while the dominant CO consumption reaction is R99. The reaction rate profiles also indicate that at low pressures (p = 5 atm) there is consumption of CO in the region downstream of the rich premixed zone. This is mainly due to reaction R99, which is exothermic and consumes CO in this region. At high pressures (p = 20 atm), however, the reaction rate profiles indicate a CO production region between the two reaction zones, which is shown more clearly in Figure 12d. As indicated in Figure 12d, the dominant CO production reactions in this region are R140, R166, and R167. As noted earlier, reaction R140 is also associated with the observed endothermicity in this region. Moreover reaction R99, which consumes CO, becomes less significant in this region at high pressures (p = 20 atm) due to the reduced OH concentration. This further contributes to the observed endothermic behavior and increase in CO concentration in this region at high pressures.

To summarize, our simulations of high-pressure methane-air PPFs indicate that as the pressure is increased above a critical value of 11 atm, the flame structure changes significantly. At low pressures (p < 11 atm), the region between the two reaction zones is characterized by transport processes with negligible chemical activity. However, at high pressures (p > 11 atm), this region is characterized by significant chemical activity that involves endothermicity and production of CO. The endothermicity reduces temperature in this region, and is mainly due to reactions R140 and R84, with R84 occurring in the reverse direction, while the production of CO in this region is caused by reactions R140, R166, and R167. As the pressure is increased further, both the endothermicity and production of CO become more significant and occur over a larger region. This may be an important result since it implies that interactions between the two reaction zones change markedly as the pressure is increased above a critical value. It has also implications regarding the effect of pressure on flame stability and emission characteristics of PPFs.

Pathway Analysis

The ROPA algorithm (Turanyi, 2003) was employed to characterize the effect of pressure on the dominant reaction pathways for methane-air PPFs. The flames were simulated using the GRI-3.0 mechanism for the base case for p = 1 and 20 atm. There are two well-known pathways for methane oxidation, namely the C_1 and C_2 paths (Dupont et al., 1998; Li et al., 1999) In general, methane reacts with H, OH and O producing the methyl radical (CH_3), which then follows two major paths, namely C_1 path and C_2 paths, leading to the formation of CO. CO
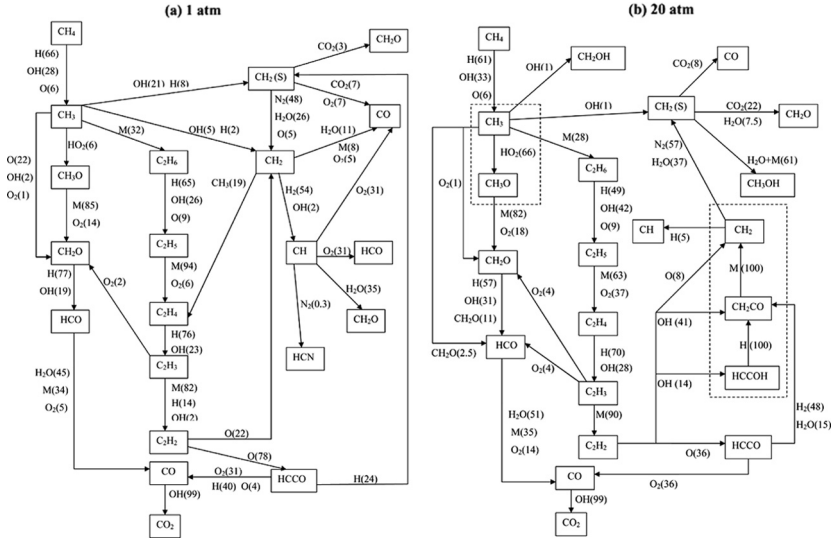
Figure 13. Reaction pathways for methane-air PPFs established at $\phi = 1.4$, $a_s = 100\,s^{-1}$ and p = 1 atm (a) and 20 atm (b) computed using GRI 3.0 mechanism. The effect of pressure on the dominant pathways is highlighted by dotted boxes in Figure 13b.

formed is subsequently oxidized to CO_2 mainly through its reaction with OH radical. The dominant pathways for PPFs established at 1 and 20 atm are shown in Figure 13. The numbers in the parenthesis represent the percentage conversion of a reactant to product by a specific species.

In the C_1 path, the conversion of CH_3 to CO involves two major routes. The first one involves the conversion of CH_3 to CH_2O that forms CHO, which is then converted to CO. CH_3 also reacts with HO_2 to form CH_3O, which then forms CH_2O. The second route involves the conversion of CH_3 to CH_2 and $CH_2(S)$, both of which produce CO directly as well as through CH, as indicated in Figure 13. In the C_2 path, two CH_3 radicals combine to produce C_2H_6, which forms C_2H_5, which then leads to the formation of C_2H_2 through C_2H_4 and C_2H_3. C_2H_2 is then oxidized to produce (1) CH_2 that forms CH and then CO, and (2) HCCO that forms CO. The CH radicals also react with N_2 to form HCN, which leads to the formation of prompt NO (not shown). The results for p = 1 atm shown in Figure 13a are generally in good agreement with those reported by Li et al. (1999), except that the conversion of CH_2 to CH is overpredicted in the present study, which is based on the GRI 3.0 mechanism. This is in accord with the investigations of Naha et al. (2004) and Ravikrishna et al. (2000), who observed that GRI 3.0 overpredicts CH and thereby prompt NO compared to that predicted by GRI 2.11.

The comparison of the dominant reaction pathways at 1 atm and 20 atm leads to the following observations:

1. As p increases, the C_1 path becomes relatively more important than the C_2 path. For example, at 1 atm 68% of CH_3 is consumed by C_1 path and 32% by C_2 path, whereas at 20 atm, 72% of CH_3 is consumed by C_1 path and 28% by C_2 path. This is mainly due to reaction (R119) $CH_3 + HO_2 \rightarrow CH_3O + OH$, which becomes important at high pressures, and is indicated by a dotted box in Figure 13b. The increase in HO_2 concentration at high pressure is a well-known feature of H_2-O_2 chemistry (Briones et al., 2004).

2. At 1 atm, within the C_1 path, 31% of CH_3 is consumed by the CH_2O route, and 36% by the CH_2 route. At 20 atm, however, the CH_2O route becomes much more significant, consuming 70% of CH_3, while the CH_2 route becomes irrelevant. This is again due to reaction (R119) $HO_2 + CH_3 \rightarrow OH + CH_3O$, and is consistent with the results reported by Rozenchan et al. (2002).

3. At 20 atm new reaction pathways leading to the formation of CH_2CO from C_2H_2 become important, as indicated by a dotted box in Figure 13b. As discussed earlier, the conversion of CH_2CO to CO through reaction R140 is an important contributor to the observed endothermicity and production of CO in the region between the reaction zones.

4. The amount of CH_2 converted to CH is reduced from 56% to 5% as the pressure is increased from 1 to 20 atm. This would significantly reduce the amount of prompt NO produced at high pressures. Since the maximum flame temperature does not vary appreciably with pressure, the amount of thermal NO is not expected to change significantly. Hence, the total NO is expected to decrease at elevated pressures.

Effects of Equivalence Ratio and Strain Rate on High-Pressure PPFs

Simulations were performed to characterize the effect of ϕ and a_s on the PPF structure at high pressure. Figure 14 presents temperature profiles for PPFs established at $\phi = 1.7$, $a_s = 100 \, s^{-1}$, and different pressures. These profiles are qualitative similar to those for the base case ($\phi = 1.4$ and $a_s = 100 \, s^{-1}$), except that the separation distance between the reaction zones is reduced at higher ϕ, since the rich premixed zone moves closer to the nonpremixed zone. This is due to the fact that the flame speed associated with the rich premixed decreases as ϕ is increased. A more important observation from Figure 14 is that similar to the base case, the temperature profiles for $\phi = 1.7$ indicate a region of endothermicity between the reaction zones. However, the critical pressure for

Figure 14. Temperature profiles for methane-air PPFs established at $\phi = 1.7$ and $a_s = 100\,s^{-1}$ for different pressures.

endothermicity to appear increases from 11 atm to 18 atm, as ϕ is increased from 1.4 to 1.7.

Figure 15 presents temperature profiles for PPFs established at $\phi = 1.4$, $a_s = 150\,s^{-1}$, and different pressures. These profiles are qualitatively

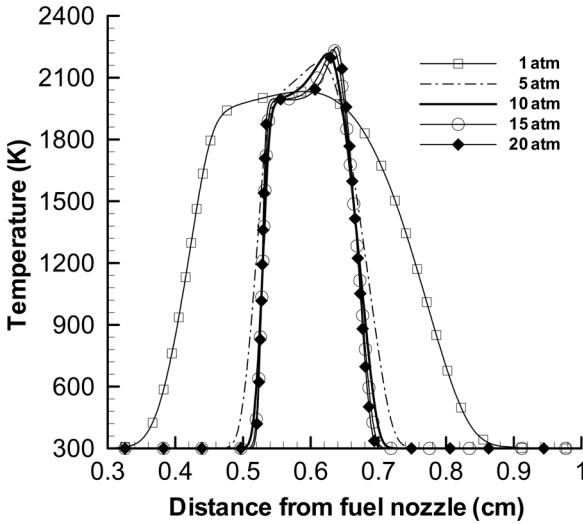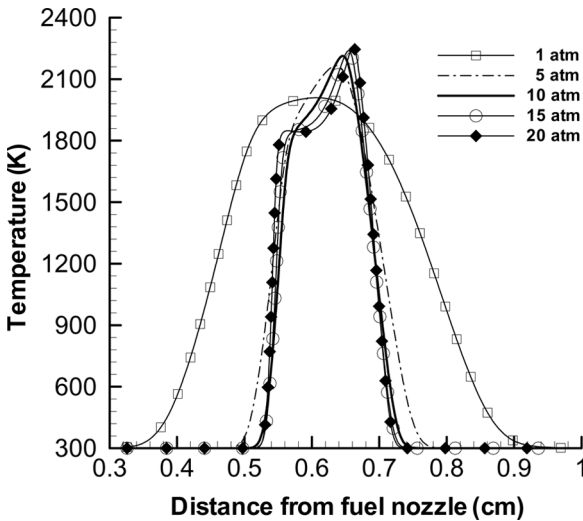**Figure 15.** Temperature profiles for methane-air PPFs established at $\phi = 1.4$ and $a_s = 150\,s^{-1}$ for different pressures.

similar to those for $\phi = 1.4$ and $a_s = 100\,s^{-1}$, except that the separation distance between the reaction zones is reduced for the higher strain rate case. Since the fuel stream velocity increases as the strain rate is increased, the premixed reaction zone is located further downstream in order to achieve a balance between flame speed and local flow velocity. The temperature profiles again indicate a region of endothermicity between the reaction zones at high pressures. However, the critical pressure for endothermicity to appear increases from 11 atm to 18 atm, as a_s is increased from 100 to $150\,s^{-1}$. To summarize, the effect of increasing ϕ and/or a_s is to reduce the separation distance between the reaction zones, and increase the critical pressure for endothermicity to appear.

CONCLUSIONS

We have presented a numerical investigation of counterflow methane-air partially premixed flames (PPFs) at high pressure. Four different mechanisms, namely the GRI-2.11, the GRI-3.0, the San Diego, and the C_2 mechanisms have been examined, and the effect of pressure on the PPF structure has been characterized. Important observations are as follows:

1. For the pressure range investigated (p = 1 to 20 atm), there is excellent agreement between the measured and predicted flame speeds using the four mechanisms. However, there are noticeable differences in the PPF structures computed using these mechanisms at high pressures. These differences are clearly highlighted by the comparison of heat release rate profiles. Thus, a PPF represents a very effective crucible for evaluating various reaction mechanisms at high pressure.

2. The GRI-3.0 mechanism has been used to characterize the effect of pressure on the PPF structure. At low pressures, the PPF exhibits a typical double flame structure that consists of rich premixed and non-premixed reaction zones. As the pressure is increased, the separation distance between the reaction zones initially decreases (for $p \leq 10$ atm) and then becomes nearly constant at higher pressures. This is mainly due to the effect of pressure on the flame speed associated with the rich premixed zone.

3. At low pressures, the region between the reaction zones is characterized by transport processes with negligible chemical activity. However, as the pressure exceeds a certain critical value, this region is characterized by significant chemical activity that involves endothermicity and production of CO. The endothermicity reduces temperature in this region, and is caused by reactions R140:

CH_2CO $(+M) \Leftrightarrow CH_2 + CO$ $(+M)$ and R84 (occurring in the reverse direction): $OH + H_2 \Leftrightarrow H + H_2O$. The production of CO is caused by reactions R140, R166: $HCO + H_2O \Leftrightarrow H + CO + H_2O$, and R167: $HCO + M \Leftrightarrow H + CO + M$. The critical pressure at which the endothermicity and production of CO are first observed increases as ϕ and/or a_s are increased. Moreover, as the pressure is increased above the critical value, both the endothermicity and production of CO become more significant and occur over a larger region. This is an important result and highlights the need for experimental investigations of methane-air PPFs, and the validation/development of high-pressure methane-air chemistry models using such flames. It also has implications regarding the effect of pressure on the stability and emission characteristics of PPFs, which are strongly influenced by interactions between the two reaction zones.

4. The effect of pressure on the dominant reaction pathways has been characterized. Results indicate that at high pressure, C_1 path becomes more important compared to C_2 path, and within the C_1 path, the consumption of CH_3 via CH_3O route becomes much more significant than that via CH_2 route. In addition, new reaction pathways leading to the formation of CH_2CO from C_2H_2 become important at high pressure. These effects can be attributed to the fact that and species HO_2 and CH_2OH become important at high pressure.

5. Thermal radiation is found to have a negligible effect on the computed flame structure for the range of conditions investigated.

REFERENCES

Aung, K.T., Hassan, M.I., and Faeth, G.M. (1998) Effect of pressure and nitrogen dilution on flame/stretch interactions of laminar premixed $H_2/O_2/N_2$ flames. *Combust. Flame*, **112**, 1–15.

Azzoni, R., Ratti, S., Aggarwal, S.K., and Puri, I.K. (1999) The structure of triple flames stabilized on a slot burner. *Combust. Flame*, **119**, 23–40.

Barlow, R.S., Karpetis, A.N., Frank, J.H., and Chen, J.Y. (2001) Scalar profiles and NO formation in laminar opposed-flow partially premixed methane/air flames. *Combust. Flame*, **127**, 2102–2118.

Bennett, B.A.V., Mcenally, C.S., Pfefferle, L.D., and Smooke, M.D. (2000) Computational and experimental study of axisymmetric coflow partially premixed methane/air flames. *Combust. Flame*, **123**, 522–546.

Blevins, L.G. and Gore, J.P. (1999) Computed structure of low strain rate partially premixed CH_4/air counterflow flames: Implications for NO formation. *Combust. Flame*, **116**, 546–566.

Bowman, C.T., Hanson, R.K., Davison, D.F., Gardiner, W.C., Lissianski, V., Smith, G.D., Golden, D.M., Frenklach, M., and Goldenberg, M. (1995) Available at: <http://www.me.berkeley.edu/gri_mech/>.

Briones, A.M., Puri, I.K., and Aggarwal, S.K. (2004) Effect of pressure on counterflow hydrogen air partially premixed flame. *Combust. Flame.*, **140**, 46–59.

Chemical-Kinetic Mechanisms for Combustion Applications (2003) The San Diego Mechanism homepage: <http://maeweb.ucsd.edu/~combustion/cermech/>.

Choi, C.W. and Puri, I.K. (2001) Contribution of curvature to flame-stretch effects on premixed flames. *Combust. Flame*, **126**, 1640–1654.

Dupont, V. and Williams, A. (1998) NO_x mechanisms in rich methane-air flames. *Combust. Flame*, **114**, 103–118.

Egolfopoulos, F.N. and Law, C.K. (1990) Chain mechanisms in the overall reaction orders in laminar flame propagation. *Combust. Flame*, **80**, 7–16.

Flynn, F.F, Durrett, R.P., Hunter, G.L., Loye, A.O.Z., Akinyemi, O.C., Dec, J.E., and Westbrook, C.K. (1999) An integrated view combining laser diagnostics, chemical kinetics, and empirical validation. *Diesel Combustion: Paper 99-01-0509*, SAE.

Fotache, C.G., Sung, C.J., Sun, C.J., and Law, C.K. (1998) Mild oxidation regimes and multiple criticality in nonpremixed hydrogen-air counterflow. *Combust. Flame*, **112**, 457–471.

Gardiner, W.C. (1984) *Combustion Chemistry*. Springer-Verlag, New York.

Gore, J.P. and Zhan, N.J. (1996) NO_x emission and major species concentrations in partially premixed laminar methane/air co-flow jet flames. *Combust. Flame*, **105**, 414–418.

Gu, X.U., Haq, M.Z., Lawes, M., and Woolley, R. (2000) Laminar burning velocity and Markstein length of methane-air mixtures. *Combust. Flame*, **121**, 41–58.

Halter, F., Chauveau, C., Chaumeix, N.D., and Gokalp, I. (2004) Characterization of the Effects of Pressure and Hydrogen Concentration on Laminar Burning Velocities of Methane-Hydrogen-Air Mixtures, *Proc. Combust. Instit.*, **30**, 201–208.

Hassan, M.I., Aung, K.T., and Faeth, G.M. (1998) Measured and predicted properties of laminar premixed methane/air flames at various pressures. *Combust. Flame*, **115**, 539–550.

Jomaas, G., Zheng, X.L., Zhu, D.L., and Law, C.K. (2004) Experimental Determination of Counterflow Ignition Temperatures and Laminar Flame Speeds of C_2–C_3 Hydrocarbons at Atmospheric and Elevated Pressures, *Proc. Combust. Instit.*, **30**, 193–200.

Kee, R.J., Rupley, F.M., Meeks, E., and Miller, J.A. (1996) A Fortran Chemical Kinetics Package for the Analysis of Gas Phase Chemical Plasma Kinetics, Report No. SAND96-8216, Sandia National Laboratories.

Konnov, A.A. (2000) Detailed reaction mechanism for small hydrocarbons combustion. Release 0.5 homepage: <http://homepages.vub.ac.be/~akonnov/>.

Kwon, O.C. and Faeth, G.M. (2001) Flame/stretch interactions of premixed hydrogen-fueled flames: Measurements and predictions. *Combust. Flame*, **124**, 590–610.

Kwon, O.C., Rozenchan, G., and Law, C.K. (2002) Cellular Instabilities and Self-Acceleration of Outwardly Propagating Spherical Flames, *Proc. Combust. Instit.*, **29**, 1775–1783.

Lee, B.J. and Chung, S.H. (1997) Stabilization of lifted tribrachial flames in a laminar nonpremixed jet. *Combust. Flame*, **109**, 163–172.

Leis, A.P. and Strechlow, R.A. (1969) On the propagation of turbulent flames. *Combust. Flame*, **13**, 111–129.

Li, S.C. and Williams, F.A. (1999) NO_x formation in two-stage methane-air flames. *Combust. Flame*, **118**, 399–414.

Lockett, R.D., Boulanger, B., Harding, S.C., and Greenhalgh, D.A. (1999) The structure and stability of the laminar counterflow partially premixed methane/air triple flame. *Combust. Flame*, **119**, 109–120.

Lutz, A.E., Kee, R.J., Grcar, J.F., and Rupley, F.M. (1996) A Fortran program for calculating opposed flow diffusion flames. Report No. SAND96-8243, Sandia National Laboratories.

Markstein, G.H. (1964) *Non-Steady Flame Propagation*. Pergamon, New York, p. 22.

Naha, S., Briones, A.M., and Aggarwal S.K. (2005) Effects of fuel blends on pollutant emissions in flames. *Submitted to Comb. Sci. Tech.*, **177**, 183–220.

Papas, P., Glassman, I., and Law, C.K. (1994) Effects of Pressure and Dilution on the Extinction of Counterflow Nonpremixed Hydrogen-Air Flames, *Proc. Combust. Instit.*, **25**, 1333–1339.

Park, J., Lee, K., and Lee, E. (2001) Effects of ambient pressure on flame structure of $CO/H_2/N_2$ counterflow diffusion flame. *Inter. J. Ener. Res.*, **25**, 187–205.

Peters, N. and Rogg, B. (1993) *Reduced Kinetic Mechanism for Applications in Combustion Systems*, Springer-Verlag, New York.

Pogliani, B., Hamins, A., and Puri, I.K. (2001) Effect of Thermal Radiation on the Extinction of Diluted Counterflow Nonpremixed Flames, Fall Western States Section Meeting of the Combustion Institute at University of Utah, *Paper No. 01F-5*.

Ravikrishna, R.V. and Laurendeau, N.M. (2000) Laser-induced fluorescence measurements and modeling of nitric oxide in counterflow partially premixed flames. *Combust. Flame*, **122**, 474–482.

Rogg, B., Hehrendt, F., and Warnatz, J. (1986) Turbulent Nonpremixed Combustion in Partially Premixed Diffusion Flamelets with Detailed Chemistry, *Proc. Combust. Instit.*, **25**, 1533–1541.

Rozenchan, G., Zhu, D.L., Law, C.K., and Tse, S.D. (2002) Outward Propagating, Burning Velocities and Chemical Effects of Methane Flames up to 60 atm, *Proc. Combust. Instit.*, **29**, 1461–1469.

Shu, Z., Krass, B.J., Choi, C.W., Aggarwal, S.K., Katta, V.R., and Puri, I.K. (1998) An Experimental and Numerical Investigation of the Structure of Steady Two-Dimensional Partially Premixed Methane-Air Flames, *Proc. Combust. Instit.*, **27**, 625–632.

Shu, Z., Choi, C.W., Aggarwal, S.K., Katta, V.R., and Puri, I.K. (1999) Gravity effects of steady two-dimensional partially premixed methane-air flame. *Combust. Flame*, **118**, 91–107.

Shu, Z., Katta, V.R., Puri, I.K., and Aggarwal, S.K. (2000) Effects of C_2-chemistry on the structure of partially premixed methane-air flames. *Comb. Sci. Tech.*, **157**, 185–211.

Smith, G.P., Golden, D.M., Frenklach, M., Moriarty, N.W., Eiteneer, B., Goldenberg, M., Bowman, C.T., Hanson, R.K., Song, S., Gardiner, W.C., Lissianski, V.V., and Qin, Z. (1999) Available at: <http://www.me.berkeley.edu/gri_mech/>.

Smooke, M.D., Seshadri, K., and Puri, I.K. (1988) The Structure and Extinction of Partially Premixed Flames Burning Methane in Air, *Proc. Combust. Instit.*, **22**, 1555–1563.

Sohn, C.H. and Chung, S.H. (2000) Effect of pressure on extinction, acoustic pressure response and NO formation in diluted hydrogen-air diffusion flames. *Combust. Flame*, **121**, 288–300.

Sohn, C.H., Chung, S.H., Lee, S.R., and Kim, J.S. (1998) Structure and acoustic-pressure response of hydrogen-oxygen diffusion flames at high pressure. *Combust. Flame*, **115**, 299–312.

Sohn, C.H., Jeong, I.M., and Chung, S.H. (2002) Numerical study of the effects of pressure and air-dilution on NO formation in laminar counterflow diffusion flames of methane in high temperature air. *Combust. Flame*, **130**, 83–93.

Takagi, T. and Xu, Z. (1995) *Proceedings of the ASME-JSME Thermal Engineering Joint Conference*, **3**, 69–74.

Tanoff, M.A. and Smooke, M.D. (1996) The Sensitivity Structure of Partially Premixed Methane-Air vs. Air Counterflow Flames, *Proc. Combust. Instit.*, **26**, 1121–1128.

The leeds methane oxidation mechanism. (2001) Homepage: <http://www.chem.leeds.ac.uk/Combustion/mechanisms/metan15.dat>.

Thomsen, D.D., Kuligowski, F.F., and Laurendeau, N.M. (1999) Modeling of NO formation in premixed, high-pressure methane flames. *Combust. Flame*, **119**, 307–318.

Tse, S.D., Zhu, D.L., and Law, C.K. (2000) Morphology and Burning Rates of Expanding Spherical Flames in H_2/O_2/Inert Mixtures up to 60 Atmospheres, *Proc. Combust. Instit.*, **28**, 1793–1800.

Turanyi, T. (2005) Kinalc Homepage, <http://www.chem.leeds.ac.uk/Combustion/kinalc.htm>.

Vagelopoulos, C.M., Egolfopoulos, F.N., and Law, C.K. (1994) Further Considerations on the Determination of Laminar Flame Speeds with the Counterflow Twin-Flame Technique, *Proc. Combust. Instit.*, **25**, 1341–1347.

Xue, H.S. and Aggarwal, S.K. (2001) Effects of reaction mechanisms on structure and extinction of partially premixed flames. *AIAA J.*, **39**, 637–645.

Xue, H.S. and Aggarwal, S.K. (2002) Structure and extinction of heptane/air partially premixed flames. *AIAA J.*, **40**, 2289–2297.

Xue, H.S., Aggarwal, S.K., Osborne, R.J., Brown, T.M., and Pitz, R.W. (2002) Assessment of reaction mechanisms for counterflow methane-air partially premixed flames. *AIAA J.*, **40**, 1236–1238.

Zhu, X.L., Gore, J.P., Karpetis, A.N., and Barlow, R.S. (2002) The effects of self-absorption of radiation on an opposed flow partially premixed flame. *Combust. Flame*, **129**, 342–345.